Chinese Chemical Letters 37 (2026) 111979

Contents lists available at ScienceDirect

Chinese Chemical Letters

journal homepage: www.elsevier.com/locate/cclet

Efficient degradation of tetracycline hydrochloride *via* high-redox S-scheme MOF-on-MOF heterojunction catalyst

Yu Wang[a], Changjiang Lu[a], Danhua Jiao[b], Fei Wang[c], Xiaojian Gong[a], Tianhua Yu[a,*], Anping Wang[a,*], Chong-Chen Wang[c,*]

[a] *Key Laboratory for Information System of Mountainous Areas and Protection of Ecological Environment, Guizhou Normal University, Guiyang 550025, China*
[b] *School of Materials Science and Engineering, Guizhou Minzu University, Guiyang 550025, China*
[c] *Beijing Key Laboratory of Functional Materials for Building Structure and Environment Remediation, School of Environment and Energy Engineering, Beijing University of Civil Engineering and Architecture, Beijing 100044, China*

ARTICLE INFO

Article history:
Received 20 July 2025
Revised 2 October 2025
Accepted 15 October 2025
Available online 17 October 2025

Keywords:
S-scheme heterojunction
MOF-on-MOF
Antibiotics
Photo-Fenton

ABSTRACT

The strategic engineering of heterointerface architecture is demonstrating its critical pathway for optimizing charge dynamics in metal-organic framework (MOF)-based photo-Fenton systems. This work presents a novel ZIF-8@NH_2−MIL-101(Fe) heterostructure with precisely controlled MOF-on-MOF configuration, which exhibits exceptional catalytic performance in the degradation of antibiotics. Experimental results revealed desired catalytic capacity with 91.4 % tetracycline hydrochloride (TCH) degradation within a short time and satisfactory stability across pH 3.0–9.0 under visible light irradiation ($\lambda \geq 420$ nm). Ecotoxicological assessment exhibits that the ecological risks of degradation intermediates diminish significantly when compared with those of the parent TCH. Comprehensive mechanistic investigation indicates that TCH decomposition is governed by superoxide radical ($^{\bullet}O_2^-$) and hydroxyl radical ($^{\bullet}OH$) as the primary reactive species. The proposed S-scheme charge transfer mechanism is verified by Mott–Schottky analysis and in X-ray photoelectron spectroscopy. Meanwhile, the enhanced interfacial charge separation efficiency is confirmed by electrochemical impedance spectroscopy. This work not only advances the development of Fe-based MOF heterojunctions for photo-Fenton catalysis but also provides critical insights into the relationship between heterostructure engineering and catalytic efficiency.

© 2026 Published by Elsevier B.V. on behalf of Chinese Chemical Society and Institute of Materia Medica, Chinese Academy of Medical Sciences.

Antibiotics have been extensively used as fundamental therapeutic agents in modern medicine since their discovery. However, the indiscriminate overuse of these pharmacological compounds in clinical and agricultural practices has resulted in the widespread accumulation of antibiotic residues in ecological systems, which has emerged as a pressing global health concern that demands urgent interdisciplinary intervention [1,2]. Tetracycline hydrochloride (TCH) residues are resistant to degradation due to their stable chemical structures [3], posing a potential threat to both ecosystems and human health [4–6]. Consequently, developing efficient degradation methods for TCH residues has become a priority in environmental remediation research. Various biological, physical, and chemical methods have been employed to treat wastewater contaminated with antibiotic residues. In contrast, advanced oxidation processes (AOPs) can completely mineralize pollutants into CO_2 and H_2O or degrade them into small molecules, which are considered one of the effective methods for treating recalcitrant pollutants.

The Fenton reaction is an effective AOP, in which a series of reactive oxygen species (ROSs) (*e.g.*, $^{\bullet}O_2^-$, $^{\bullet}OH$, and $^{\bullet}OOH$) are generated through the redox reaction of Fe^{2+} and H_2O_2 for the non-selective degradation of organic pollutants [7]. However, traditional homogeneous Fenton systems face several drawbacks in practical use, such as a limited pH range, substantial iron ion leaching, and the creation of secondary pollutants [8]. In contrast, environmentally friendly photocatalytic reactions typically occur under mild conditions and do not produce secondary pollutants. Photo-Fenton technology integrates Fenton and photocatalysis, using light energy to boost ROS generation *via* the redox reaction of Fe^{2+} and H_2O_2, thus enhancing organic pollutant degradation. However, the development of catalysts with strong visible light response and efficient charge separation is a key factor restricting the development of photo-Fenton technology. Constructing heterojunctions to enhance the utilization efficiency of photogenerated electrons is an effective

* Corresponding authors.
E-mail addresses: tianhua@gznu.edu.cn (T. Yu), anping-wang@gznu.edu.cn (A. Wang), wangchongchen@bucea.edu.cn (C.-C. Wang).

https://doi.org/10.1016/j.cclet.2025.111979
1001-8417/© 2026 Published by Elsevier B.V. on behalf of Chinese Chemical Society and Institute of Materia Medica, Chinese Academy of Medical Sciences.

approach to enhance overall catalytic efficiency of photo-Fenton system [9,10].

Metal-organic frameworks (MOFs) are characterized by large specific surface area, highly porous framework, and customizable structure [11], making them promising candidates for applications in drug delivery [12], electrochemistry [13], water treatment [14], catalysis [15], and other fields. Among them, NH_2−MIL-101(Fe) is a representative heterogeneous photo-Fenton catalyst, featuring abundant Fe–O and –NH_2 functional groups [16]. For instance, Guo *et al.* [17] constructed NH_2−MIL-88B(Fe)/TiO_{47}/PAN electrostatically spun nanofibrous membranes for the degradation of chlortetracycline (CTC) with a degradation efficiency of 94.9 %. However, a significant challenge of single MOF materials is the rapid recombination of photogenerated charge carriers. To enhance photo-Fenton catalysis efficiency and broaden the light absorption range of the catalyst, a high-redox potential is required. The construction of heterojunctions by combining different materials can effectively prolong charge carrier lifetimes. Recently, the fabrication of MOF-on-MOF heterojunctions by conjugating two different MOFs has attracted increasing attention. A heterojunction of MOF-on-MOF type with an S-scheme, characterized by the presence of an internal electric field and interfacial chemical bonding, was fabricated by integrating NH_2−MIL-125(Ti) and ZIF-67(Co) with CoFe Prussian blue analogs *via* an ion exchange process. This heterojunction exhibited high efficiency in the photocatalytic degradation of antibiotic compounds [18]. By growing another MOF with a stable structure and better photocatalytic performance on the MOF surface, ZIF-67(Co) and ZIF-8(Zn) were selectively grown on a cake-shaped MIL-125(Ti) substrate to form a ternary MOF-on-MOF heterojunction [19]. This close interfacial contact can more effectively promote charge separation and carrier transfer, thereby greatly improving the catalytic efficiency [20]. The synthesized composites have suitable redox potentials, wide light absorption ranges, and the effective avoidance of photogenerated carrier recombination. Therefore, the construction of heterojunctions with MOF-on-MOF structures has tremendous potential to improve photocatalytic performance.

In this work, solvothermal epitaxial method was employed to grow ZIF-8(Zn) as the guest on the NH_2−MIL-101(Fe) host (Fig. 1a). A MOF-on-MOF S-scheme heterojunction of ZIF-8@NH_2−MIL-101(Fe) was designed to provide a suitable bandgap and high redox potential. Experimental results revealed that the synthesized composite demonstrated a strong response to visible light and expected catalytic performance for TCH degradation. Furthermore, a possible photocatalytic mechanism was explored through comprehensive characterizations. The study also conducted a systematic evaluation of the degradation mechanism of TCH and the toxicity of its degradation products.

The supporting materials (Texts S1 and S2 in Supporting information) provide detailed information about the raw materials for catalysts synthesis and the instrumentation employed for characterizations. In this study, different catalysts were synthesized using the solvothermal method (Text S3 in Supporting information). The morphological characteristics of the catalyst were analyzed using scanning electron microscopy (SEM) and high-resolution transmission electron microscopy (HRTEM). NH_2−MIL-101(Fe) exhibits an irregular polyhedral structure (Fig. 1b), while pure ZIF-8 has a smooth surface with a regular polyhedral structure (Fig. 1c). Through a MOF-on-MOF growth strategy, ZIF-8@NM (1.0:4.0) was formed by the epitaxial growth of ZIF-8 on the surface of NH_2-MIL-101(Fe). SEM images reveal that ZIF-8@NM(1.0:4.0) possesses a corncob-like morphology (Fig. 1d). The HRTEM images further indicate that small particles are attached to and have grown on the surface, forming an overall spindle-shaped architecture reminiscent of a corncob (Figs. 1e and f). As shown in Fig. 1f, ZIF-8@NM(1.0:4.0) is composed of different crystals. ZIF-8@NM(1.0:4.0) shows lattice

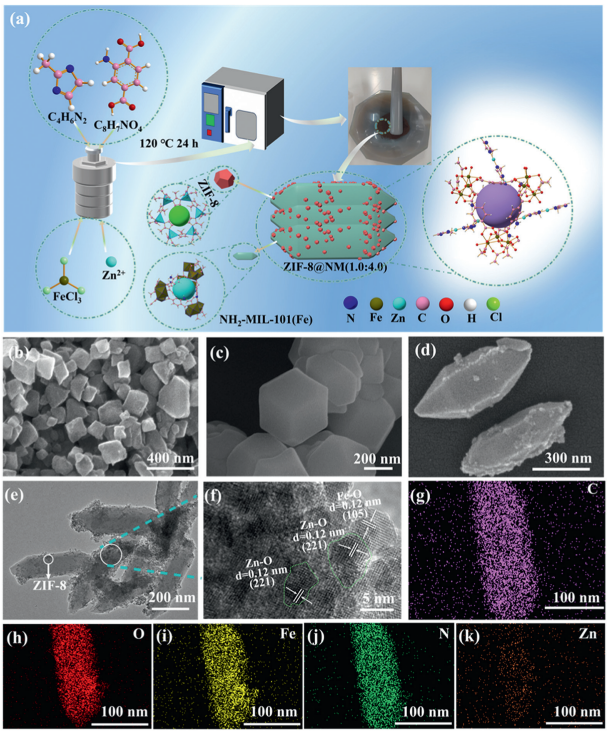


Fig. 1. (a) Preparation flowchart of the catalysts. (b-d) SEM images of NH_2−MIL-101 (Fe), ZIF-8 and ZIF-8@NM(1.0:4.0). (e, f) HRTEM image of ZIF-8@NM(1.0:4.0). (g-k) EDS elemental scans of ZIF-8@NM(1.0:4.0).

fringes with a *d*-spacing of 0.12 nm, corresponding to the (221) and (105) crystal plane of Zn-O and Fe-O, respectively, confirming the successful fabrication of the MOF-on-MOF composite materials. In addition, the energy dispersive X-ray spectroscopy (EDS) elemental distributions show the homogeneous distribution of Fe, Zn, C, N, and O across the particle surfaces (Figs. 1g–k and Fig. S1 in Supporting information).

X-ray diffraction (XRD) was used to characterize the crystal structures of as-synthesized catalyst (Fig. 2a). ZIF-8 exhibits characteristic diffraction peaks at $2\theta = 7.4°$, 10.4°, 12.8°, 16.6°, 22.2°, and 26.7°, while NH_2−MIL-101(Fe) exhibits characteristic diffraction peaks at $2\theta = 9.1°$, 16.5°, 18.8°, 21.7°, 25.2°, and 28.7°, consistent with previous reports [21,22]. The XRD spectra of ZIF-8@NM composites with different ratios show distinct characteristic diffraction peaks from both single MOFs, confirming the successful formation of the heterostructures. Fourier-transform infrared (FT-IR) spectroscopy further verified the composite structure, with all materials exhibiting characteristic organic ligand vibrations in the range of 1100–1750 cm^{-1} (Fig. 2b) [23–25]. In addition to the characteristic peaks of organic ligands, a strong Zn–O peak at 530.7 cm^{-1} is also observed from ZIF-8@NM [26,27]. N_2 adsorption–desorption was conducted to evaluate the specific surface areas and porosity of the materials. The adsorption–desorption isothermal curves of ZIF-8@NM(1.0:4.0), ZIF-8, and NH_2−MIL-101(Fe) display type H1 hysteresis loops according to the IUPAC classification, confirming the microporous structure (Fig. 2c, Figs. S2a and b in Supporting information) [28,29]. The specific surface areas of NH_2−MIL-101(Fe), ZIF-8@NM(1.0:4.0), and ZIF-8 are 70.71, 150.9, and 1224.6 m^2/g, respectively. Due to the inherent microporous structure of ZIF-8, the incorporation of ZIF-8 onto NH_2−MIL-101(Fe) introduce additional micropores, resulting in a larger specific surface area of the composite material (Table S1 in Supporting information) [30].

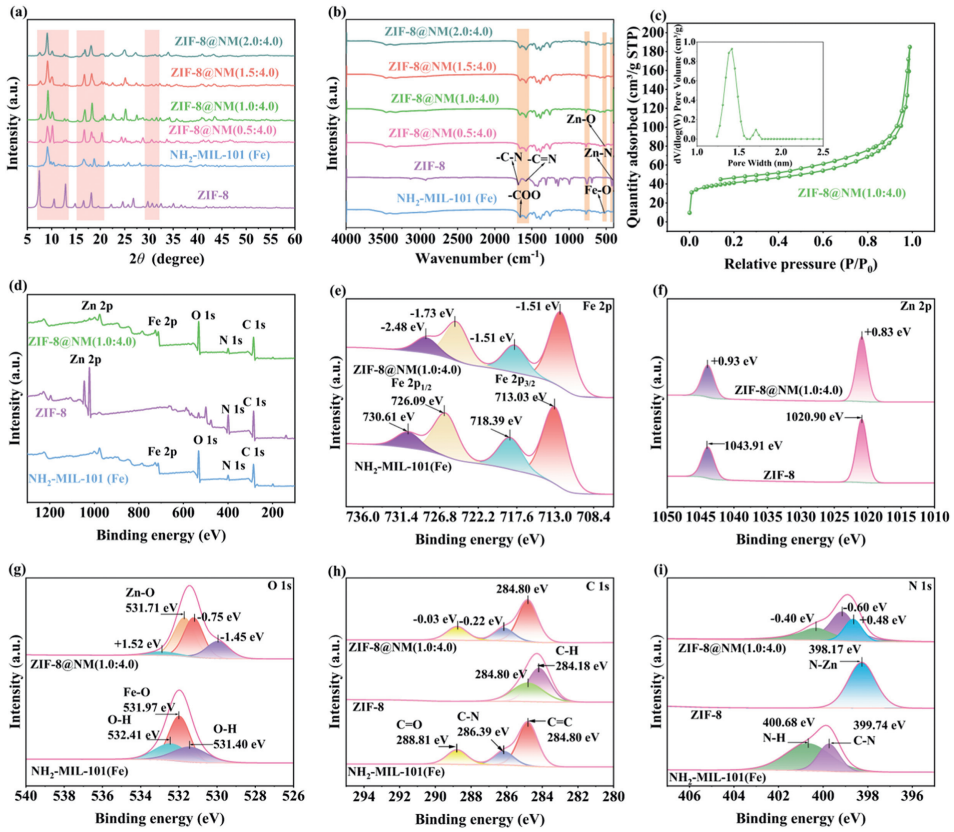


Fig. 2. (a) XRD spectra of the catalysts. (b) FT-IR spectra of the catalysts. (c) N_2 adsorption–desorption isotherms of ZIF-8@NM(1.0:4.0). (d) XPS full spectrum of the catalyst. (e) Fe 2p, (f) Zn 2p, (g) O 1s, (h) C 1s, (i) N 1s for the ZIF-8@NM(1.0:4.0).

The surface electronic structure and elemental chemical states of the catalyst were systematically investigated by X-ray photoelectron spectroscopy (XPS). The full-scan energy spectrum of the catalyst reveals the presence of C, N, O, Zn, and Fe, which agrees well with EDS mapping results (Fig. 2d). As exhibited in Fig. 2e, the binding signals at 713.03 and 726.09 eV and the satellite peaks at 718.39 and 730.61 eV in NH_2−MIL-101(Fe) are assigned to Fe^{3+} species [31,32]. The Fe 2p peaks in ZIF-8@NM(1.0:4.0) exhibit an overall blue shift, indicating modified local electronic environments of the surface Fe atoms [33]. The binding energies at 1020.90 and 1043.91 eV are attributed to Zn $2p_{3/2}$ and Zn $2p_{1/2}$ of ZIF-8 (Fig. 2f) [34]. Compared with ZIF-8, the binding energy of the Zn $2p_{3/2}$ and Zn $2p_{1/2}$ orbitals in ZIF-8@NM(1.0:4.0) show a noticeable red shift. The composite exhibit a Zn–O binding energy at 531.71 eV [35], while the Fe–O binding energy blue-shifted to 531.22 eV (Fig. 2g). Slight shifts are also observed for C–N (blue shift to 286.17 eV) and N–Zn (red shift to 398.65 eV) species (Figs. 2h and i). These results suggest an increased electron density around Fe and a decreased electron density around Zn at the heterojunction interface, affirming the existence of an internal electric field.

The photon capture efficiency of the as-prepared catalysts was examined by UV-vis diffuse reflectance spectroscopy (UV-vis DRS) in the 200–800 nm wavelength range. As illustrated in Fig. 3a, ZIF-8 exhibits light absorption below 400 nm, whereas NH_2−MIL-101(Fe) and ZIF-8@NM with varying ratios display significant absorption across both the UV and visible regions. All composites exhibit a certain degree of red-shifting compared to the single Fe-MOF material [36]. The band gaps of ZIF-8, NH_2−MIL-101(Fe), and ZIF-8@NM(1.0:4.0) were calculated using Tauc's Eq. 1 to be 5.00, 1.79, and 2.00 eV, respectively (Fig. 3b) [37]. The band gaps of other composites are shown in Figs. S3a–c (Supporting information). ZIF-8@NM(1.0:4.0) exhibits a broader band gap compared to NH_2−MIL-101(Fe), primarily attributed to mid-gap states generated by surface-induced structural reconstruction of the ZIF-8 component. Photoluminescence (PL) spectra (Fig. 3c) reveal the lowest emission intensity for ZIF-8@NM(1.0:4.0), suggesting the longest lifetime of photogenerated electron–hole pairs and their suppressed recombination [38]. The charge separation and transfer abilities were measured using the electrochemical impedance spectroscopy (EIS) and transient photocurrent measurements. ZIF-8@NM(1.0:4.0) composite exhibit significantly stronger photocurrent response than the single components (Fig. S3d in Supporting information), which can be attributed to the improved separation capacity of photogenerated charge carriers [39]. Moreover, the smallest arc radius of ZIF-8@NM(1.0:4.0) indicat the superior electron transmittance (Fig. 3d) [40]. As shown in Mott–Schottky plots in Figs. 3e and f, both materials display n-type semiconductor behavior with positive slopes [41]. Meanwhile, according to Eqs. 2 and 3, the corresponding flat band potentials (E_{FB}) and conduction band energies (E_{CB}) were calculated and converted [42,43]. The E_{CB} of ZIF-8 and NH_2−MIL-101(Fe) were −0.12 and −0.74 eV, respectively. According to the theory of energy band structure, when different catalysts come into contact, the difference in the work functions (Φ) leads to electron transfer [44]. Ultraviolet photoelectron spectroscopy (UPS) was used to measure the Φ values of the two individual MOFs, and the cutoff energies (E_{cutoff}) were calculated to be 17.16 and 17.36 eV for ZIF-8 and NH_2−MIL-101(Fe), respectively (Figs. 3g and h). Using the formula $\Phi = 21.22\,eV - E_{cutoff}$, the Φ values with respect to a vacuum for ZIF-8 and NH_2−MIL-101(Fe) were calculated to be 4.06 and 3.86 eV, the Fermi energy level ($E_f = -\Phi$) for NH_2−MIL-101(Fe) (−3.86 eV *vs.* vacuum) was more negative than that of ZIF-8 (−4.06 eV *vs.* vacuum), respectively, suggesting energy band bending at the heterojunction interface

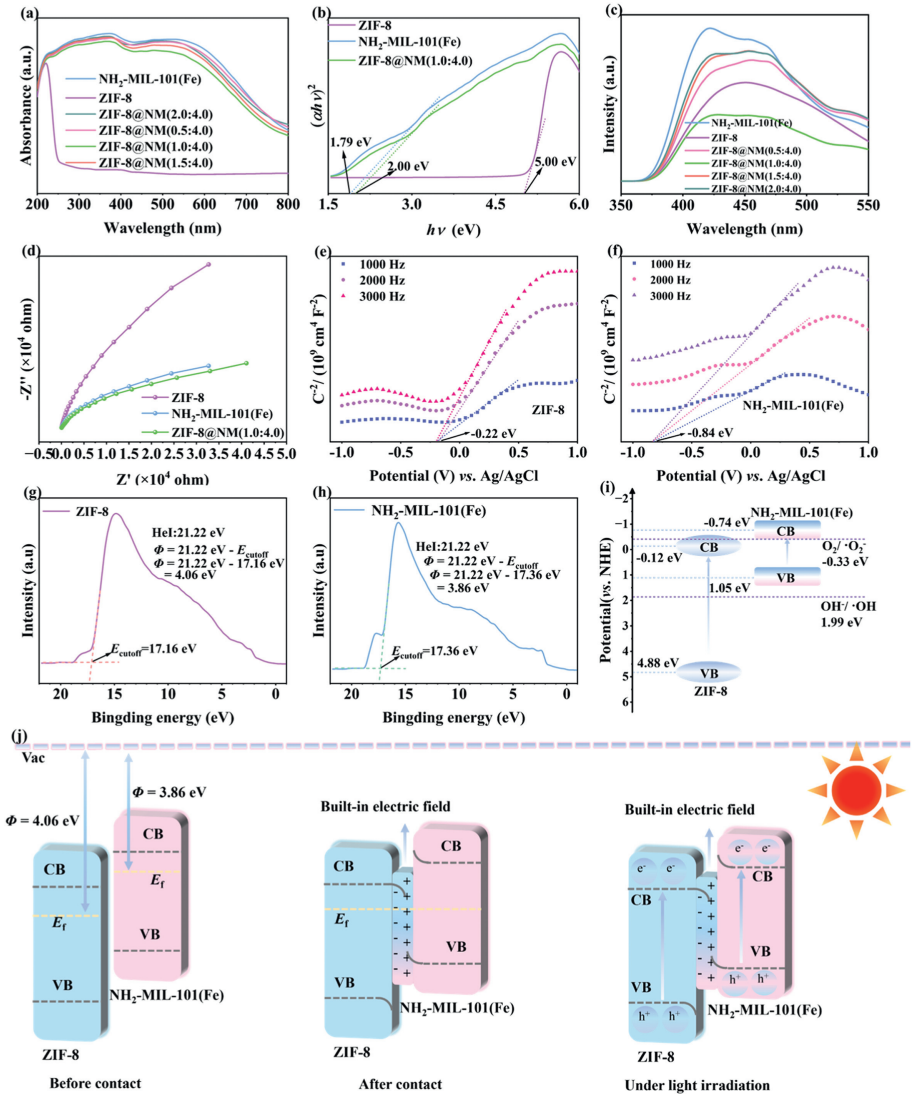


Fig. 3. (a) UV–vis diffuse reflectance spectra, (b) band gaps, and (c) photoluminescence spectra of the catalysts. (d) Electrochemical impedance spectroscopy Nyquist plot for different catalysts. (e) Mott–Schottky diagrams of ZIF-8. (f) Mott–Schottky diagrams of NH_2−MIL-101(Fe). (g) UPS spectrum of ZIF-8. (h) UPS spectrum of NH_2-MIL-101(Fe). (i) Energy band structure of ZIF-8 and NH_2−MIL-101(Fe). (j) Schematic diagram of the work function.

[45,46]. Kelvin probe force microscopy (KPFM) was further employed to investigate the local surface potential variation of the catalyst (Fig. S4 in Supporting information). For ZIF-8@NM(1.0:4.0), a pronounced reduction of 11.4 eV in the line-scan surface potential was observed under visible light illumination compared to dark conditions, confirming the transfer of photogenerated electrons from ZIF-8 to NH_2-MIL-101(Fe) upon visible-light excitation. Based on these results, the charge transfer mechanism of the ZIF-8@NM(1.0:4.0) S-scheme heterojunction catalyst was proposed in Figs. 3i and j. When ZIF-8 formed a heterojunction interface with NH_2−MIL-101(Fe), electrons migrated directionally from ZIF-8 to NH_2−MIL-101(Fe) until their Fermi levels align, facilitating efficient charge separation and enhanced photocatalytic activity.

$$(\alpha h\nu)^2 = A\left(h\nu - E_g\right) \quad (1)$$

$$E_{NHE} = E_{Ag/AgCl} + 0.1976 \quad (2)$$

$$E_g = E_{VB} - E_{CB} \quad (3)$$

where α is the absorption coefficient, h is Planck's constant, ν is the optical frequency, and E_g is the band gap.

Details of the photocatalytic experiments are provided in Text S4 (Supporting information). The spontaneous degradation of TCH was negligible in the absence of both the photo-Fenton catalyst and H_2O_2 (Blank and Blank-1). The degradation kinetics follow *pseudo*-first-order kinetics $-\ln C/C_0 = kt$, where k represents the rate constant and t is the reaction time [47]. Based on the *quasi*-first-order kinetic results (Figs. S5a and b), the k values for the five catalysts are summarized in Table S2 (Supporting information). When the proportion of ZIF-8 is too high, mass transfer may be hindered due to its large specific surface area. Conversely, the electronic modulation effect becomes insufficient when the proportion is too low, leading to inadequate catalytic performance. Considering the common synergistic effect of the two metals during the photo-Fenton reaction, ZIF-8@NM(1.0:4.0) was selected as the optimal catalyst for the subsequent one-way experiments (Fig. 4a). The experimental data show a noticeable positive correlation between the catalyst dosage and TCH removal efficiency (Fig. 4b). Therefore, in view of the costs, 0.1 g/L was determined to be the optimal catalyst dosage for the experiments. As the H_2O_2 concentration increased from 100 μL/L to 400 μL/L, the TCH removal efficiency are improved from 85.4 % to 92.8 % within 90 min (Fig. 4c). Higher concentration of H_2O_2 could improve the contact between H_2O_2

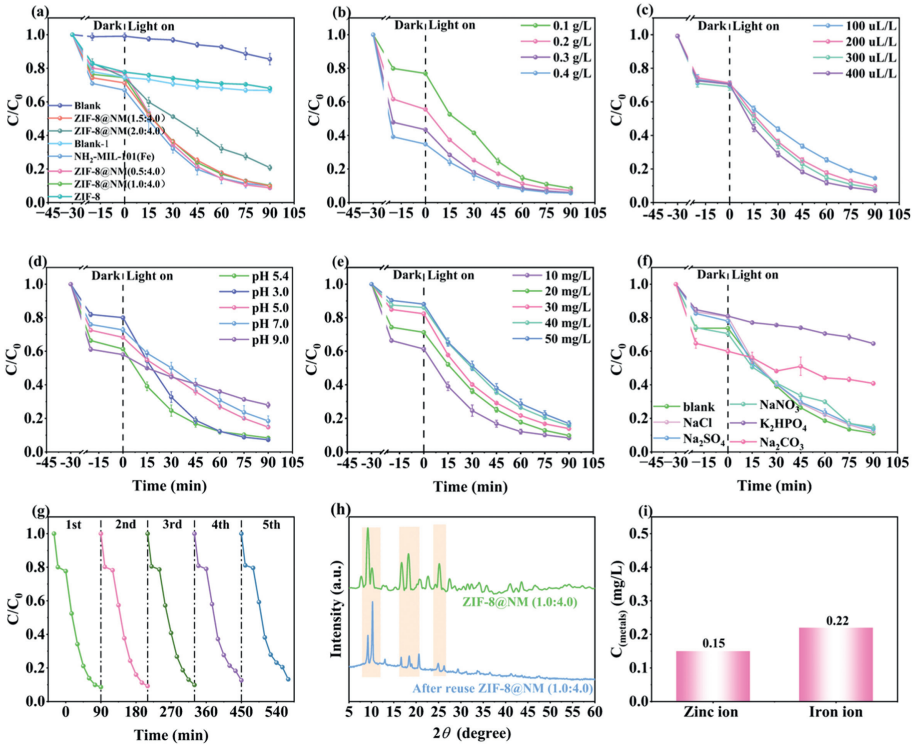


Fig. 4. (a) Performance of various catalysts in TCH degradation. (b) Plot of ZIF-8@NM(1.0:4.0) dosing. (c) Effects of H_2O_2 concentration and (d) initial pH on TCH degradation. (e) Impact of TCH initial concentration on catalytic degradation. (f) Effects of different anions on TCH degradation. (g) Cycling stability test of the catalyst for TCH degradation. (h) Comparison of the XRD patterns of the ZIF-8@NM(1.0:4.0) catalyst before and after the cycling tests. (i) Metal ion leaching concentration.

and the catalyst, generating more reactive species ($^{\bullet}OH$ and $^{\bullet}O_2^-$) to improve the degradation efficiency for TCH. However, excessive H_2O_2 would result in a self-quenching behavior and cause structural declination, thereby preventing appreciable enhancement in degradation efficiency. Thus, the operational H_2O_2 concentration was optimized at 200 μL/L, with reagent cost being the primary selection criterion. The influence of the initial pH level on the efficiency of TCH removal is shown in Fig. 4d. The degradation efficiencies at reaction times of 75 min to 90 min are similar. The highest degradation rate (92.7 %) is achieved at pH 3.0, likely due to facilitated formation of $^{\bullet}OH$ from H_2O_2 by photogenerated electrons under acidic environment as detailed in Eq. 4. At near-neutral pH 5.4), the efficiency of TCH degradation is comparable to that observed in conditions of acidity. In the present work, the catalytic system demonstrates broad applicability, with degradation efficiencies reaching up to 70 % in both acid and alkaline systems.

Actual wastewater discharges contain varying concentrations of TCH, so the initial concentration from TCH can also significantly affect the degradation process. At 10 mg/L TCH, the catalyst can achieve a degradation efficiency of 91.6 %, whereas a fivefold concentration increase (50 mg/L) resulted in a reduced efficiency of 83.1 % (Fig. 4e). Therefore, highly efficient treatment of high-concentration TCH holds practical application value. The existence of inorganic anions in water may potentially affect the catalytic efficiency. Thus, the effects of various anions (5 mmol/L Cl^-, SO_4^{2-}, NO_3^-, $H_2PO_4^-$, and CO_3^{2-}) on TCH degradation were investigated [28]. As displayed in Fig. 4f, Cl^-, SO_4^{2-}, and NO_3^- show weak inhibitory effects, while $H_2PO_4^-$ and CO_3^{2-} cause more significant suppression of TCH degradation. Notably, $H_2PO_4^-$ can react with $^{\bullet}OH$ to produce HPO_4^- with lower oxidizing capacity, as shown in Eq. 5 [48]. Furthermore, CO_3^{2-} can also interact with reactive radicals to form $^{\bullet}CO_3^-$, a substance with a lower redox potential, thereby altering the pH of the reaction system, as illustrated in Eqs. 6 and 7 [49,50].

$$H_2O_2 + H^+ + e^- \rightarrow H_2O + {}^{\bullet}OH \quad (4)$$

$${}^{\bullet}OH + H_2PO_4^- \rightarrow H_2PO_4^{\bullet} + OH^- \quad (5)$$

$$CO_3^{2-} + {}^{\bullet}OH \rightarrow {}^{\bullet}CO_3^- + H_2O \quad (6)$$

$$CO_3^{2-} + h^+ \rightarrow {}^{\bullet}CO_3^- + H^+ \quad (7)$$

To comprehensively evaluate the repeatability and sustainability of the ZIF-8@NM(1.0:4.0) catalyst, five repeated cycle experiments were conducted. As shown in Fig. 4g, ZIF-8@NM(1.0:4.0) maintains a TCH degradation rate of 86.7 % after five cycles, indicating the favorable reusability. Structural evolution of the ZIF-8@NM(1.0:4.0) catalyst after cycling was evidenced by the disappearance of the characteristic (110) diffraction peak at $2\theta = 7.4°$ in XRD patterns (Fig. 4h), suggesting pore geometry modification under repeated catalytic conditions. However, the other major characteristic diffraction peaks show no significant changes before and after cycling, further indicating the acceptable structural stability of the catalytic system. ICP-MS measurements were carried out to investigate the Leaching risks of photo-Fenton system. As depicted in Fig. 4i, zinc (1.0 mg/L) and iron (0.3 mg/L) concentrations after reaction are consistently below thresholds mandated in national water quality standard (GB 3838–2002).

Liquid chromatography–mass spectrometry was used to analyze the potential intermediates formed during the degradation reactions. The mass-to-charge ratios of some intermediates are presented in the supplementary materials (Fig. S6a in Supporting information). The three potential pathways for TCH degradation by ZIF-8@NM(1.0:4.0) are shown in Fig. S6b (Supporting information). TCH contains several sites vulnerable to radical attack, including

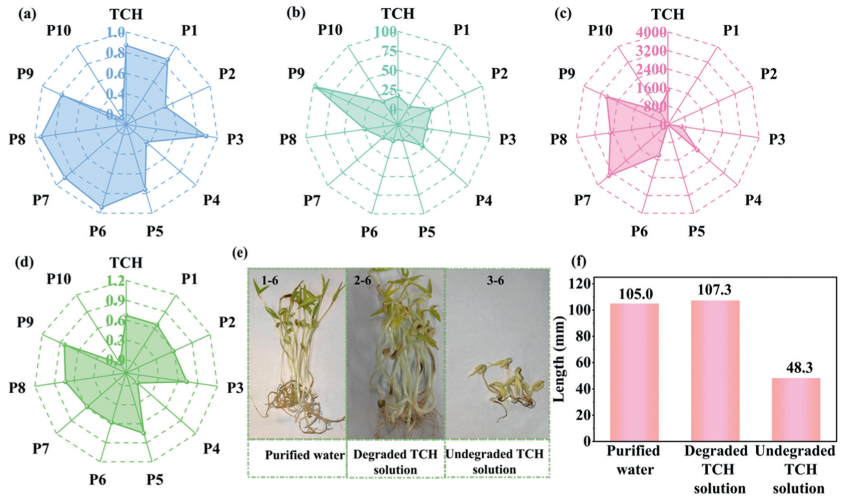


Fig. 5. (a) Developmental toxicity, (b) *daphnia magna* (LC50) (48 h), (c) oral rat LD50, (d) mutagenicity of the different intermediates. (e) Growth of mung bean sprouts subjected to different irrigation solutions. (f) Effect of different irrigation solutions on the length of mung bean sprouts.

the double bond, phenol group, and amine group. The major reactions occurring in Pathway I are as follows. First, TCH undergoes carboxylation, deamination, and decarboxylation to generate **P1** (*m/z* 413) [51]. Then, **P1** undergoes demethylation to generate **P2** (*m/z* 385). Subsequently, $^{\bullet}O_2^-$ readily attacks the oxygen-containing moiety for dehydration and decarboxylation to generate the product **P3** (*m/z* 302). Finally, **P3** undergoes a gradual process involving dealkylation, dihydroxylation, and ring-opening reactions, ultimately converting into the product **P4** (*m/z* 136) [52]. In pathway II, TCH is dehydrated by $^{\bullet}O_2^-$ attack on the oxygen-containing group and simultaneously demethylated to produce **P5** (*m/z* 391) [53]. Then, **P5** undergoes dehydroxylation and amidation reaction pathways, generating the product **P6** (*m/z* 384). **P6** is then demethylated under free radical attack and undergoes deamidation and hydroxylation, gradually transforming into the intermediate **P7** (*m/z* 343). In pathway III, $^{\bullet}OH$ readily attacks the –N–CH_3 group, leading to the demethylation reaction of TCH to generate **P8** (*m/z* 400). The carbon–oxygen ring in **P8** is then cleaved by oxidation *via* $^{\bullet}O_2^-$ attack to generate the product **P9** (*m/z* 377) [54]. Then, **P9** undergoes complex oxidative processes, such as ring-opening, dihydroxylation, and deamidation, to produce **P10** (*m/z* 138) [55]. Through subsequent oxidative reactions, the pathway-derived products are transformed into less toxic metabolites (**P4**, **P9**) with lower molecular weights. These compounds can ultimately be mineralized into inorganic end products, including CO_2 and H_2O [56].

Following photo-Fenton oxidation degradation, the intermediates generated *via* the three proposed pathways exhibit lower toxicity than the parent TCH (Figs. 5a–d). Notably, intermediates **P4** and **P10** showed "developmentally nontoxicity". After oxidization by free radicals, several intermediate byproducts demonstrate attenuated toxicity profiles, with **P4** and **P10** becoming "non-mutagenic". Overall, the toxicity assessment confirm that the photo-Fenton catalytic process can effectively mitigate the ecological risks posed by TCH. To systematically assess the ecological safety of the degradation products, the growth of mung beans was monitored in pure water, TCH solution, and treated TCH solution. Although mung beans germinate in the original TCH solution, significant growth inhibition is observed by day 6 (Fig. 5e and Fig. S7 in Supporting information). In contrast, mung beans germinate and grow well in the pure water and degraded solutions. As shown in Fig. 5f, stem elongation exhibits remarkable differences among treatments. The growth of mung beans in pure water (105.0 mm) and the degraded TCH solution (107.3 mm) was significantly greater than that in the untreated TCH solution (48.3 mm).

Electron paramagnetic resonance (EPR) and radical trapping experiments were performed to investigate the reactive oxygen species generated during the reaction process. In this experiment, methanol (MeOH) was selected as the trapping agent to h^+, L-histidine (L-His) for $^{\bullet}OH$, and sodium oxalate ($Na_2C_2O_4$) for $^{\bullet}O_2^-$, respectively. The addition of these free radical trapping agents inhibits the degradation efficiency of TCH to varying degrees. To further investigate the dominant reactive species in the system, ammonium oxalate (AO), *tert*–butanol (TBA), and *p*-benzoquinone (*p*-BQ) were selected as quenchers for h^+, $^{\bullet}OH$, and $^{\bullet}O_2^-$, respectively. As shown in Figs. S8a and b (Supporting information), the inhibitory effects of the different quenchers on the reaction were found to be largely comparable. In addition, 1,3-dimethyl-5-pyrazolone and 2,2,6,6-tetramethoxypyridine oxide (TEMPO) were employed as selective trapping agents, and the presence of the $^{\bullet}O_2^-$, $^{\bullet}OH$ and h^+ reactive species during the reaction process was analyzed by EPR (Figs. 6a–c). No signals corresponding to $^{\bullet}OH$ or $^{\bullet}O_2^-$ were detected at the beginning of the reaction. However, both radical species were observed within 5 min under standard reaction conditions, and prolonging the irradiation time beyond 10 min led to enhanced signal intensities, indicating that $^{\bullet}OH$ and $^{\bullet}O_2^-$ radicals were continuously generated throughout the photo-Fenton reaction process. Due to its intrinsic paramagnetism, TEMPO, when utilized as an h^+ trapping agent, exhibited a spontaneous EPR signal in dark conditions (Fig. 6c). With the extension of light irradiation time during the photo-Fenton reaction, h^+ generated on the catalyst surface combined with the single electrons of TEMPO, causing the amount of the trapping agent to decrease. Consequently, the longer the light time was, the weaker the EPR signal became [57]. Consistent with the EPR analysis, the use of radical scavengers in the trapping experiments confirm the presence of reactive species. These results verify that $^{\bullet}OH$ and $^{\bullet}O_2^-$ served as the primary oxidative species responsible for pollutant degradation across all reaction stages.

To investigate the catalytic capabilities of ZIF-8@NM(1.0:4.0) more precisely, charge density differences were computed using density functional theory (DFT). Detailed calculation parameters are provided in Text S5 (Supporting information), with an isosurface value set at 0.005 e/Å^3. As shown in Fig. 6d, the electron accumulation regions are shown in yellow, while the dissipation regions are shown in blue. The results suggest the occurrence of dynamic charge transfer between the Fe–O and Zn–N sites.

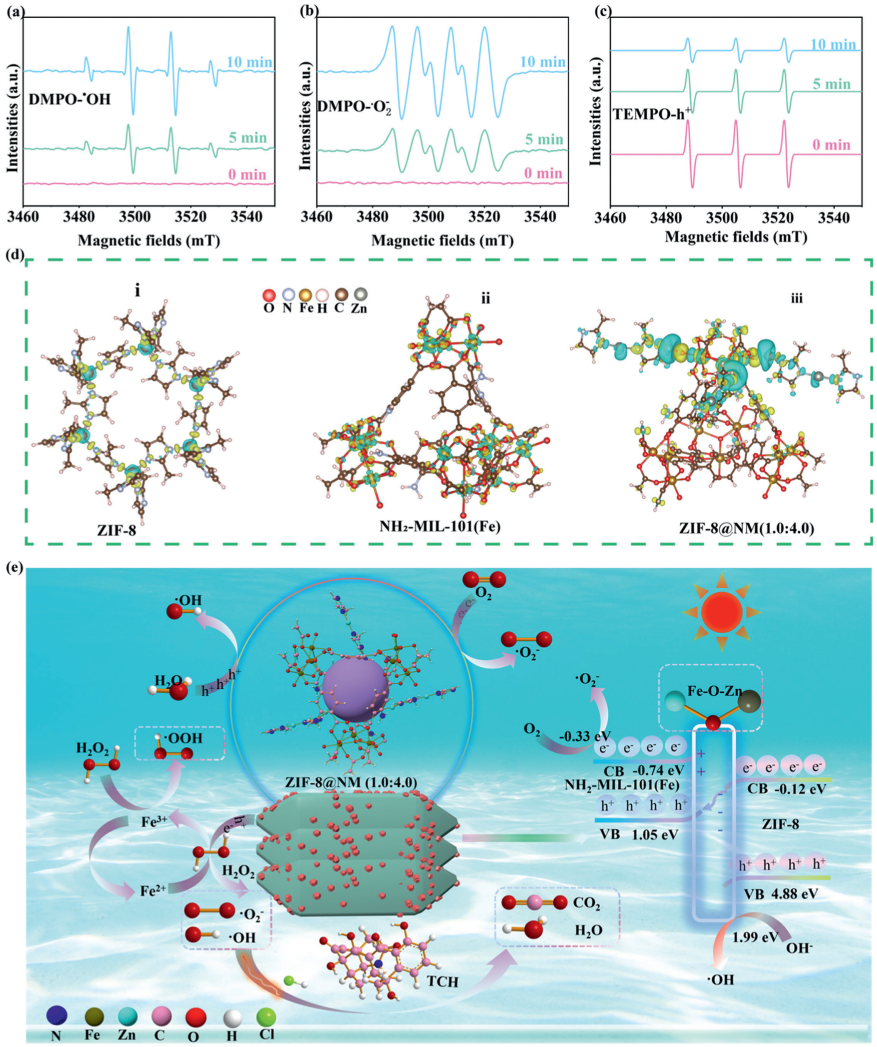


Fig. 6. (a) EPR detection spectra of ·OH. (b) EPR detection spectra of $^{\bullet}O_2^-$. (c) EPR detection spectra of h^+. (d) Differential charge density map of catalysts. (e) Mechanism diagram for simulated photo-Fenton catalytic reaction.

As exhibited in Fig. 6d-iii, the dissipation of electrons around Zn and the accumulation of electrons around Fe can be observed in ZIF-8@NM(1.0:4.0). The dynamics of charge transfer are probably originated from the formation of Fe–O–Zn bonds, which facilitates the establishment of an S-scheme heterojunction, as evidenced by multiple characterization analyses.

A possible reaction mechanism was proposed based on experiments and DFT calculations (Fig. 6e). The E_{VB} of ZIF-8 (4.88 eV *vs.* NHE) has sufficient energy to drive the h^+ to oxidize OH^- into ·OH ($E_{OH^-/\bullet OH}$ = 1.99 eV *vs.* NHE) [58]. Simultaneously, the E_{CB} (−0.74 eV *vs.* NHE) of the conduction band (CB) of NH_2−MIL-101(Fe) has a sufficient thermodynamic driving force to reduce O_2 to $^{\bullet}O_2^-$ ($E_{O_2/\bullet O_2^-}$ = −0.33 V *vs.* NHE) [59,60], during which Fe^{2+} is oxidized to Fe^{3+}. In addition, the e^- can migrate from the CB of ZIF-8 to the valence band (VB) of NH_2−MIL-101(Fe) and directly recombine with h^+ at the heterojunction interface. This interfacial charge transfer effectively suppresses the recombination of photogenerated charge carriers, thereby facilitating the reduction of Fe^{3+} ions to form catalytically active Fe^{2+} ions. This process also aids in establishing an efficient Fe^{3+}/Fe^{2+} redox cycle system. As a result, the generation of reactive oxygen species is significantly enhanced, leading to improved photocatalytic performance. Overall, the charge transfer behavior in the photo-Fenton system aligned more closely with the characteristics of an S-scheme heterojunction.

In summary, a heterojunction material composed of ZIF-8 was effectively fabricated at the interface of the NH_2−MIL-101(Fe) subsatrate *via* a straightforward solvothermal epitaxial growth method. The resulting MOF-on-MOF photocatalyst with an S-scheme heterojunction structure exhibits a degradation efficiency reaching 91.4 % within 90 min under visible light irradiation. Notably, the catalyst maintained acceptable catalytic degradation activity across a wide pH range (3–9), demonstrating excellent environmental adaptability. The level of toxicity in the intermediate products formed were considerably reduced compared to the initial pollutant. In addition, the primary active substances interacting with TCH during the reaction were detected to be $^{\bullet}O_2^-$ and ·OH. The enhanced catalytic activity is attributed to the tightly connected interface and the regulated electronic structure of Fe–O–Zn bonds. The rational construction of the S-scheme heterojunction effectively suppressed the recombination of photogenerated charge carriers through the formation of a stable internal electric field. This study offers a practical approach for designing S-scheme heterojunction catalysts to enhance TCH degradation, offering new insights into wastewater treatment *via* the photo-Fenton process under real sunlight conditions.

Declaration of competing interest

The authors declare that they have no known competing financial interests or personal relationships that could have appeared to influence the work reported in this paper.

CRediT authorship contribution statement

Yu Wang: Writing – original draft, Validation, Software, Resources, Methodology, Investigation. **Changjiang Lu:** Investigation, Formal analysis, Data curation. **Danhua Jiao:** Software, Resources, Formal analysis, Data curation. **Fei Wang:** Software, Methodology, Investigation, Data curation. **Xiaojian Gong:** Supervision, Software, Resources, Data curation. **Tianhua Yu:** Writing – review & editing, Resources, Project administration, Conceptualization. **Anping Wang:** Writing – review & editing, Supervision, Project administration, Funding acquisition, Data curation, Conceptualization. **Chong-Chen Wang:** Writing – review & editing, Conceptualization.

Acknowledgments

This work is supported by the project of Guizhou Provincial Graduate Student Research Fund (No. 2024YJSKYJJ162), the Guizhou Provincial Department of Science and Technology Projects (Nos. Qiankehe Jichu-ZK [2024] 055, Qiankehe Zhicheng [2023] 078, and Qiankehe Pingtai-KXJZ [2024] 029), and the National Natural Science Foundation of China (No. 22466011).

Supplementary materials

Supplementary material associated with this article can be found, in the online version, at doi:10.1016/j.cclet.2025.111979.

References

[1] X. Chen, R.T. Guo, W.-g. Pan, et al., Appl. Catal. B: Environ. 318 (2022) 121839.
[2] Y. Wu, X. Li, H. Zhao, et al., Chem. Eng. J. 426 (2021) 131255.
[3] J. Cai, S. Liu, Y.B. Man, et al., Chem. Eng. J. 507 (2025) 160725.
[4] H. Hu, H. Lin, X. Chen, et al., Chem. Eng. J. 476 (2023) 146682.
[5] L. Jin, Y. Huang, H. Liu, et al., J. Hazard. Mater. 463 (2024) 132904.
[6] Y. Mo, Y. Wang, L. Wang, et al., J. Hazard. Mater. 495 (2025) 138800.
[7] L. Liu, M. Chen, X. Wei, et al., Sep. Purif. Technol. 353 (2025) 128537.
[8] X. Wu, Q. Zhao, F. Guo, et al., Carbon 183 (2021) 628–640.
[9] Z. Cao, Y. Zhao, Z. Zhou, Q, et al., Appl. Surf. Sci. 590 (2022) 153081.
[10] D. Xing, Z. Cui, Y. Liu, Z, et al., Appl. Catal. B: Environ. 290 (2021) 120029.
[11] Z. Ling, Y. Gu, B. He, et al., Sep. Purif. Technol. 349 (2024) 127841.
[12] S. Ghosh, J. Krishnan, S.S. Hossain, A. Dhakshinamoorthy, S. Biswas, ACS Appl. Mater. Interfaces 15 (2023) 26843–26851.
[13] Y. Wang, Z. Liu, Z. Zhao, et al., Chem. Eng. J. 499 (2024) 156279.
[14] F. Ahmadijokani, A. Ghaffarkhah, H. Molavi, et al., Adv. Funct. Mater. 34 (2024) 2305527.
[15] K.A. Adegoke, N.W. Maxakato, Mater. Today Energy 21 (2021) 100816.
[16] A. Rajan, C. Yazhini, M. Dhileepan, B. Neppolian, Chemosphere 352 (2024) 141473.
[17] R. Guo, W. Qin, B. Wang, et al., Sep. Purif. Technol. 351 (2024) 128059.
[18] L. Yuan, C. Zhang, Y. Zou, et al., Adv. Funct. Mater. 33 (2023) 2214627.
[19] C. Liu, Q. Sun, L. Lin, et al., Nat. Commun. 11 (2020) 4971.
[20] T. Gao, H. Zhang, X. Zhao, et al., Appl. Surf. Sci. 651 (2024) 159227.
[21] L. Wu, H. Fu, Q. Wei, et al., Environ. Sci. Pollut. Res. 28 (2021) 5218–5230.
[22] K. Vinothkumar, R.G. Balakrishna, Appl. Catal. B: Environ. 340 (2024) 123199.
[23] J. Wang, W. Wang, Y. Deng, et al., Sep. Purif. Technol. 340 (2024) 126840.
[24] N. Zhang, M. Liu, Y. Wang, et al., Mater. Today Energy 38 (2023) 101419.
[25] Y. Bao, H. Ru, Y. Wang, et al., Adv. Funct. Mater. 34 (2024) 2314611.
[26] H. Tong, R. He, G. Chen, et al., J. Colloid Interface Sci. 671 (2024) 732–741.
[27] P. Cai, N. Zhang, Y. Wang, et al., Sep. Purif. Technol. 362 (2025) 131872.
[28] X. Zheng, Z. Yang, G. Zeng, et al., Chem. Eng. J. 505 (2025) 159865.
[29] H. Yang, Y. Wan, Q. Cheng, H. Zhou, Z. Pan, Dalton Trans. 51 (2022) 15080–15088.
[30] M. Hu, D. Zhao, X. Yan, et al., Appl. Catal. B: Environ. 362 (2025) 124753.
[31] A. Singh, A. Bhatnagar, A.K. Gupta, Sep. Purif. Technol. 363 (2025) 132176.
[32] A. Zhang, F. Shan, Z. Zhang, et al., Sep. Purif. Technol. 344 (2024) 127212.
[33] J. Zou, Q.Q. Tang, B. Wu, et al., Appl. Catal. B: Environ. 366 (2025) 4963124.
[34] X. Li, E. Shang, J. Li, J. Tian, J. Li, Chem. Eng. J. 508 (2025) 160930.
[35] C. Adena, T. Imae, Chem. Eng. J. 506 (2025) 160037.
[36] T. Huec, A. López-Francés, I. Lázaro, et al., ACS Appl. Nano Mater. 18 (2024) 20201–20212.
[37] D. Sun, D. Chu, M. Xu, C. Xing, L. Ling, J. Hazard. Mater. 496 (2025) 139422.
[38] J. Yang, X. Hao, J. Liu, Z. Nan, Z. Jin, Sep. Purif. Technol. 354 (2025) 129348.
[39] J. Sun, H. Wu, C. Fu, et al., Appl. Catal. B: Environ. 351 (2024) 123976.
[40] Y. Zhang, X. Hao, M. Lu, et al., Nano Energy 136 (2025) 110762.
[41] P. Chen, Z. Zhu, Z. Liu, et al., Chem. Eng. J. 506 (2025) 159689.
[42] R. Yang, Q. Li, Z. Ma, et al., Chem. Eng. J. 506 (2025) 160043.
[43] Y. Zhou, X. Cui, Y. Zheng, et al., Chem. Eng. J. 507 (2025) 160549.
[44] J. Ma, A. Li, Q. Liu, et al., Appl. Catal. B: Environ. 367 (2025) 125101.
[45] F. Wang, Y. Gao, Y. Chai, et al., Appl. Catal. B: Environ. 364 (2025) 124848.
[46] Y. Chai, F. Wang, Y. Gao, et al., Environ. Res. 282 (2025) 122099.
[47] M.Y. Sun, L. Zhang, Y. Li, Chai, et al., Chin. Chem. Lett. 36 (2025) 110035.
[48] J. Wang, J. Yao, L. Yin, et al., Chem. Eng. J. 497 (2024) 154836.
[49] X. Bai, X. Liu, R. Zong, Appl. Catal. B: Environ. 366 (2025) 125062.
[50] Z. Xu, R. Teng, L. Xu, et al., Adv. Funct. Mater. 34 (2024) 2401248.
[51] L. Sun, X. He, B. Liu, et al., Sep. Purif. Technol. 353 (2025) 128515.
[52] X. Liu, S. Chen, X. Tantai, et al., Sep. Purif. Technol. 363 (2025) 132001.
[53] S.H. Wang, M. Du, H.L. Guo, et al., J. Mater. Chem. A 13 (2025) 5860–5869.
[54] J. Fu, X. Liu, G. Huang, Z. Wang, Chem. Eng. J. 505 (2025) 159260.
[55] P. Kaur, D. Aggarwal, S. Singhal, Adv. Compos. Hybrid Mater. 8 (2025) 156.
[56] Y. Pei, A. Lei, M. Wang, et al., J. Hazard. Mater. 488 (2025) 137286.
[57] X. Hua, H. Chen, Z. Wang, et al., Sep. Purif. Technol. 347 (2024) 127632.
[58] N. Li, Y. Niu, W. An, et al., Appl. Catal. B: Environ. 369 (2025) 125141.
[59] Y. Zhang, F. Zhou, X. Ding, et al., Chem. Eng. J. 508 (2025) 160891.
[60] C. Lu, Y. Wang, Z. Yang, et al., J. Environ. Chem. Eng. 13 (2025) 118902.